Nonaxisymmetric simulations of the Princeton magnetorotational instability experiment with insulating and conducting axial boundaries

Dahan Choi, Fatima Ebrahimi, Kyle J. Caspary, Erik P. Gilson, Jeremy Goodman, and Hantao Ji

Phys. Rev. E **100**, 033116 — Published 24 September 2019

DOI: 10.1103/PhysRevE.100.033116

Non-axisymmetric Simulations of the Princeton Magnetorotational Instability (MRI) Experiment with Insulating and Conducting Axial Boundaries

Dahan Choi,[1] Fatima Ebrahimi,[1,2] Kyle J. Caspary,[2] Erik P. Gilson,[2] Jeremy Goodman,[1] and Hantao Ji[1,2]

[1] *Department of Astrophysical Sciences, Princeton University*
[2] *Princeton Plasma Physics Laboratory, Princeton University*

(Dated: May 17, 2019)

Stability and nonlinear evolution of rotating magnetohydrodynamic (MHD) flows in the Princeton magnetorotational instability (MRI) Experiment are examined using three-dimensional (3D) non-axisymmetric simulations. In particular, the effect of axial boundary conductivity on a free Stewartson-Shercliff Layer (SSL) is numerically investigated using the Spectral Finite Element Maxwell and Navier Stokes (SFEMaNS) code. The free SSL is established by a sufficiently strong magnetic field imposed axially across the differentially rotating fluid with two rotating rings enforcing the boundary conditions. Numerical simulations show that the response of the bulk fluid flow is vastly different in the two different cases of insulating and conducting endcaps. We find that for the insulating endcaps, there is a transition from stability to instability of a Kelvin Helmholtz-like mode that saturates at an azimuthal mode number $m = 1$, while for the conducting endcaps, the reinforced coupling between the magnetic field and the bulk fluid generates a strong radially localized shear in the azimuthal velocity resulting in Rayleigh-like modes even at reduced thresholds for the axial magnetic field. For reference, 3D non-axisymmetric simulations have also been performed in the MRI unstable regime to compare the modal structures.

I. INTRODUCTION

Angular momentum transport in accretion disks has been of great interest, as the gravitationally contracting material must transport angular momentum outward through means of instabilities and turbulence [1–3]. Because the specific angular momentum (Ωr^2) for these accretion disks undergoing Keplerian motion increases radially outward, accretion disks are hydrodynamically stable to Rayleigh's centrifugal instability. Although nonlinear hydrodynamic instabilities also might arise in such systems, experimental and numerical work suggest that such accretion disks are stable against purely hydrodynamic modes [4–6] in particular in the absence of special features [7] and some physical stratifications [8, 9]. Therefore, the magnetorotational instability (MRI) [10, 11], the MHD instability of a differentially rotating flow in the presence of weak magnetic field, is believed to be the driving mechanism of angular momentum transport in astronomical accretion disks [12].

In search of MRI in the laboratory, experiments have been dedicated to studying the stability of differentially rotating flows in the MHD regime. Global MHD simulations are also critical to investigate the onset and saturation of MRI in Taylor-Couette flow geometry [15–20] or in plasma [21] experiments. In particular, in order to understand the liquid-boundary interactions of the experimental apparatus, global simulations with realistic boundary conditions are crucial. In this paper, using global MHD simulations, we investigate the effect of experimental axial boundaries in the Princeton MRI experiment. The Princeton MRI experiment has been developed to demonstrate MRI in a laboratory setting using a magnetized conducting fluid (GaInSn) rotating in a modified Taylor-Couette device [13, 14].

In Taylor-Couette devices, there are hydrodynamic boundary layers that form due to differences in the rotation rate between the boundaries and interior (bulk) fluid, such as Ekman layers and Stewartson layers forming perpendicular and parallel to the rotation axis [23, 24]. These boundary layers drive nontrivial secondary circulation that modifies the bulk flow profile as a whole. The strengths of these circulations are determined by the differential rotation rates of the Taylor-Couette device. On the other hand, there are magnetic-liquid interactions that arise when an axial magnetic field is applied across the system to drive MRI, such as magnetized Ekman or Hartmann and magnetized Stewartson or Shercliff layers that form perpendicular and parallel to the background field [25, 26] in addition to MRI. Furthermore, induced current loops that close around these layers can also nontrivially affect the background flow dynamics, with the strength of these interactions determined by the fluid-boundary conductivities.

Understanding these secondary circulations is of great importance for identifying MRI in a laboratory setting. Initial experimental and computational studies [27, 28] were conducted with insulating boundaries; however, recent computational work has been carried out motivated by the change from insulating axial boundary endcaps to conducting ones. Wei *et al.* [29] discovered that changes in the radial magnetic field corresponded well to the previously calculated MRI thresholds and that the nonlinear saturation of the root mean square of total (volume averaged) radial magnetic field (the "MRI signal") had similar dependence on key parameters such as B_0, the background magnetic field, as the linear MRI growth rate. Most importantly, the simulations showed that the MRI signal with conducting axial boundaries is significantly increased [29] from the MRI signal with insulating axial boundaries. Based on these numerical predictions, the axial boundaries have been changed to copper in the present Princeton MRI experiment. Experimental studies have been recently conducted in the slow-rotation regime to understand the fluid response under the new boundary conditions [33], revealing a vastly different instability response in the two cases. Developing a thorough understanding of the full fluid response in this slow-rotation regime is essential for providing guidance for planned experiments as well as numerical calculations in the experimentally relevant fast-rotating MRI-unstable regime. Similar experimental and numerical studies [30, 31] have been conducted comparing insulating and conducting axial boundaries to understand the effects of boundary layers on the evolution of helical MRI in the Potsdam Rossendorf Magnetic Instability Experiment (PROMISE), and have led to an improved characterization of helical MRI [32].

In this paper, we utilize 3D non-axisymmetric calculations to study numerically the formation of SSLs, the resulting mode structures, and mechanism of the instabilities. We first perform simulations with the initial flow and parameter space as close as possible to the actual experiments [33] for direct comparisons. Consistent with the experimental results [33], numerical MHD simulations using the Spectral Finite Element Maxwell and Navier-Stokes solver (SFEMaNS) [22] code show that the response of the bulk fluid flow is also vastly different in the two different cases of insulating and conducting endcaps. We find that for the insulating endcaps, there is a transition from stability to instability of a Kelvin Helmholtz-like mode that saturates at an azimuthal mode number of $m = 1$, while for the conducting endcaps, the reinforced coupling between the magnetic field and the bulk fluid generates a strong shear in the azimuthal velocity resulting in Rayleigh-like modes (with hydrodynamic instability criterion for the angular momentum $\partial \mathrm{L}/\partial r < 0$) at reduced thresholds for the axial magnetic field. Good agreement between the simulations and the experimental results are obtained; for the insulating boundary experiments there is a coherent $m = 1$ instability that develops in the azimuthal flow, and for the conducting boundary experiments a strong shear profile similar to the numerical predictions is seen. We further compare the resulting mode structure of the Rayleigh-like modes in the conducting boundary simulations with the MRI mode structures in a reference simulation case.

The paper is organized as follows. The simulation method and its experimental relevance are discussed in Section II. In Section III, we present energy and eigenstructure analysis for insulating and conducting boundary conditions as well as comparisons with a reference MRI unstable case. We summarize the results in Section IV and present implications for future simulations and experimental efforts to identifying MRI in the Princeton MRI Experiment.

II. METHODS

Non-axisymmetric 3D numerical simulations were conducted with the Spectral Finite Element Maxwell and Navier-Stokes solver (SFEMaNS) [22]. The solver uses a Fourier spectral method in the azimuthal plane and a finite-element method in the meridional plane with up to 72,000 triangular finite element slices. While previous work [29] focused on axisymmetric perturbations (with only the $m = 0$ mode fully resolved), up to 16 spectral azimuthal modes are resolved here to search for non-axisymmetric shearing layer instabilities. Each instance of the 3D non-axisymmetric simulation uses 256 cores running in parallel with 2GB memory per core, and requires 3 weeks to complete.

We solve the dimensionless Navier Stokes equation in the fluid domain modeled for the Princeton MRI Experiment using a cylindrical coordinate system with the units of length, time, magnetic field, and conductivity being r_1, Ω_1^{-1}, $r_1\Omega_1\sqrt{\rho\mu_0}$, and σ with ρ and σ representing the density and conductivity. The dimensionless parameters of the system are the fluid Reynolds number $Re \equiv \Omega_1 r_1^2/\nu$ corresponding to the viscosity, the magnetic Reynolds number $Rm \equiv \Omega_1 r_1^2 \sigma_{\mathrm{GaInSn}}\mu_0$ determining the rotation rate, the Lehnert number $B_0 \equiv V_A/\Omega_1 r_1$ corresponding to the magnetic field strength with $V_A \equiv B/\sqrt{\mu_0\rho}$ the Alfven velocity, and the Elsasser number $\Lambda \equiv B_0^2 Rm$ which is the ratio of the Lorentz and Coriolis force. Figure 1 shows the simulation domain. The fluid is encapsulated in 4 rotating parts: the inner cylinder, inner ring, the outer cylinder, and the outer ring. The radii of the inner and outer cylinder are $r_1 = 7$ cm and $r_2 = 21$ cm respectively; the endcaps are divided into differentially rotating inner and outer rings to suppress secondary circulations [35]. The inner/outer ring transition radius is $r_t = 14$ cm, and the height of the fluid domain is $h = 28$ cm. The endcap thickness $d = 2$ cm determines the effective electrical thickness $\delta \equiv \sigma_{\mathrm{Cu}} d/\sigma_{\mathrm{GaInSn}}$. The induction equation is solved in the fluid/solid domain, namely the conducting fluid, the copper endcaps, and the steel inner cylinder ends. Finally, a spherical vacuum domain with radius $r_s = 280$ cm surrounds the fluid and solid domain. For the insulating endcap simulations, the induction equation is no longer solved in the solid domain and the entirety of the solid domain is incorporated into the vacuum domain, representing full insulating axial boundaries in the experiment.

We primarily perform our analysis under two different regimes of rotation rates: the slow rotation rate ($Rm \sim 0.6$) with the Split-Stable rotation profile devised to visualize the hydrodynamic response and compare with initial experimental results [33], and the fast rotation rate ($Rm \sim 10$) with the MRI rotation profile to highlight the differences in mode structure between the slowly rotating magnetohydrodynamic response and the fast rotating MRI. In the stability diagram in Figure 2, the red and blue diamonds represent the experimental and simulational parameters for the slow rotation regime

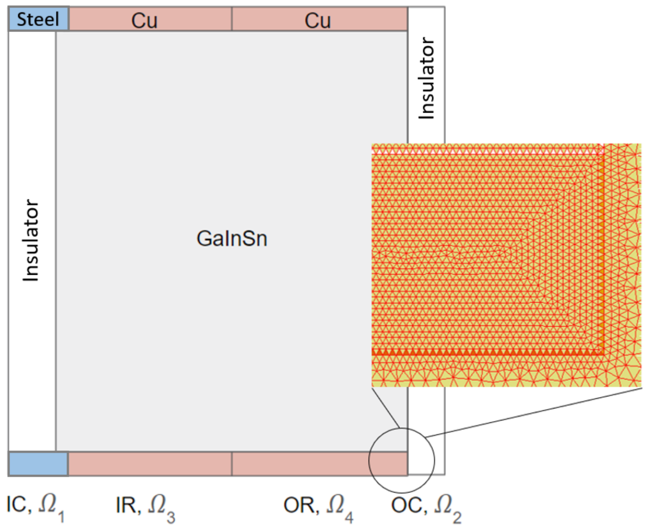

FIG. 1. Initialization of the simulation domain. The inner cylinder is composed of an insulating shell with stainless steel ends, and outer cylinder is composed of stainless steel in the experiments and an insulator in the simulations. The inner and outer rings are composed of copper. The working fluid is GaInSn.

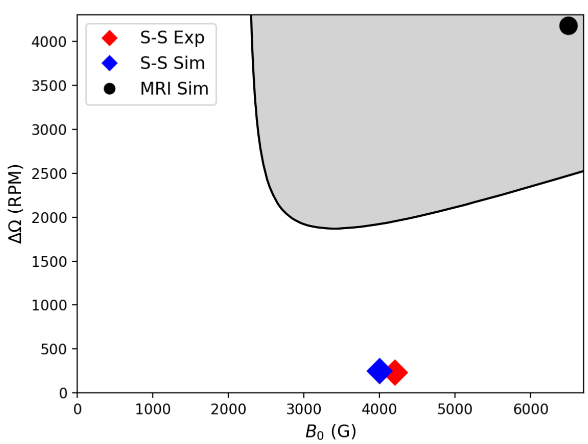

FIG. 2. Visualization of the parameter space involved in the simulations and experiments, with the curve representing marginal stability and the shaded area representing the MRI unstable regime. The red and blue diamonds respectively represent the Split-Stable experiment and simulations that were conducted in the slow-rotation regime. The black dot represents the MRI simulation in the fast-rotation regime with the background field $B_0 = 6500$ G and the differential rotation rate $\Delta\Omega = \Omega_1 - \Omega_2 = 4250$ rpm.

respectively and the black dot represents the simulational parameter for the fast rotation regime. The axial field values B_0 were chosen to amplify the fluid response in the slow rotation regime and to fully destabilize MRI in the fast rotation regime.

A "Split-Stable" (S-S) rotation profile composed of co-rotating inner and outer components respectively is enforced in the simulations to amplify the effects of the shear inside the fluid domain. The inner cylinder, inner ring, outer ring, outer cylinder rotations Ω_1, Ω_3, Ω_4, Ω_2 were configured at the relative rates $\Omega_1 = \Omega_3$, $\Omega_2 = \Omega_4 = 0.25\Omega_1$ ($\Omega_1 = 335$ rpm) for this setup with no-slip boundary conditions between ring-fluid interface. The initial bulk fluid rotations were matched to the respective ring rotations piecewise uniformly and relaxed until a hydrodynamically steady rotation profile was established to closely emulate the real experimental rotation profile. Figure 3 shows this initial background rotation profile Ω as a function of radius r at the midplane; although there are some slight discrepancies in the flow near the inner components $r = 1.25$ to $r = 1.75$, overall the experimental and simulational flow closely resemble each other in the bulk fluid. The initial flow for the simulations failed to be hydrodynamically stable for Rossby number $Ro \equiv (\Omega_1 - \Omega_2)/\Omega_2 = 2.35$ matching the experiment, so a higher differential rotation rate with $Ro = 3$ was used to develop the hydrodynamically stable initial flow in the simulations. [34].

For reference, we have also performed 3D non-axisymmetric simulations of the MRI unstable case with the "MRI" rotation profile that lead to the optimization of the MRI signal [29]. The relative rotation rates were configured at $\Omega_3 = 0.55\Omega_1$, $\Omega_4 = \Omega_2 = 0.1325\Omega_1$ ($\Omega_1 = 5000$ rpm), and the background magnetic field $B_0 = 0.2$ ($B = 6500$ G). This simulation is not exactly experimentally relevant as the background magnetic field is initialized instantaneously after the piecewise solid body ("PSB") initial state is enforced where the fluid in the entire volume has the same velocity as the rotating boundaries. However the flow responds to the applied field and relaxes rapidly before MRI growth so that the relaxed flow could be considered as the effective initial state. Figure 3b shows the rotation profiles of the piecewise solid body initial state and the relaxed flow immediately after magnetic field application.

Table I lists the experimental parameters used in the split-stable experiments [33]. The experimental parameters are normalized to the aforementioned scaling in the simulations. The dimensionless constants of the simulations and experiments are summarized in Table II. The dimensionless constants for the Split-Stable simulations and experiments are relatively similar with the exception of the fluid Reynolds number, which is $Re \sim 10^6$ in the experiments but is $Re = 1000$ in the simulations due to computational limitations.

III. SIMULATION RESULTS

Here, we present simulation results for the two cases of split-stable (S-S) case and MRI unstable case. In the split-stable configuration, the inner and outer cylinders rotate with the inner and outer rings respectively, relaxing to a flow with larger shear around the mid-radius.

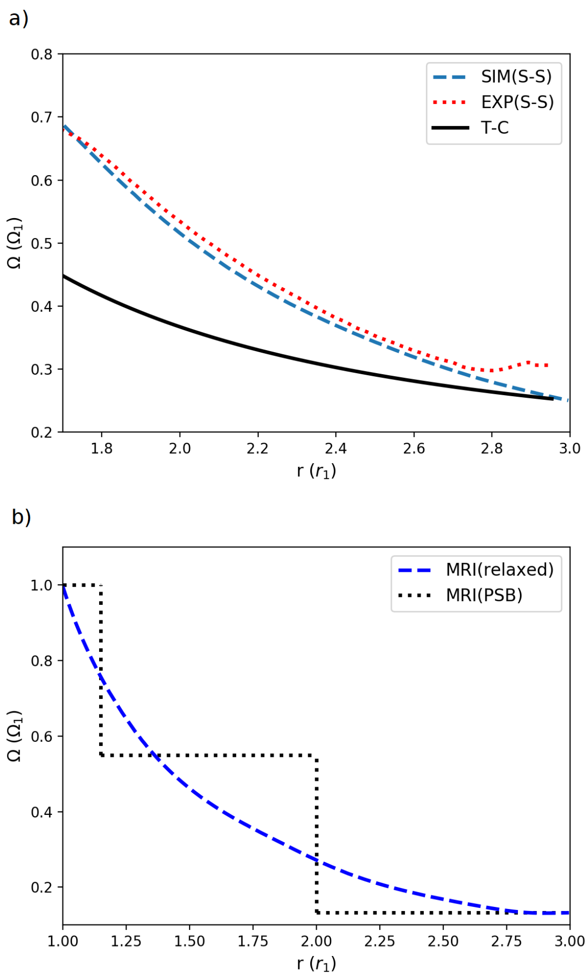

FIG. 3. Plots of the fluid rotation rate Ω as a function of radius taken at the midplane ($z = 0$) of the system. a) Initialization of the hydrodynamically stable initial state is done by relaxing a piecewise uniform state matched at the rotation rates of the boundaries to more precisely emulate real experimental fluid flows. The simulation flow for the split-stable case is indicated in a dashed blue line, the experimental flow in a dotted red line, and the ideal Taylor-Couette solution in a solid black line. The experimental flow is collected using ultrasound Doppler velocimetry (UDV) from a run with the same ratio of inner and outer components, but at a slightly higher rotation rate. b) Reference MRI unstable case with piecewise solid body initial state and the relaxed rotation profile. The relaxed rotation profile is the effective initial state, which could trigger MRI for this reference case.

The effect of insulting and conducting endcap boundaries are presented for this case. For the reference unstable MRI case, a piecewise solid body initial state (with three rotational frequencies) relaxes to a state with lower flow shear unstable to MRI. For the conducting endcap cases, the resulting mode structures and energies for the S-S case are compared with the MRI case.

Experimental Parameters Split-Stable Experiment	
r_1	6.9 cm
r_2	20.3 cm
r_t	13.5 cm
h	28 cm
d	2 cm
Ω_1, Ω_3	335 rpm
Ω_2, Ω_4	100 rpm
ρ_{Cu}	9.0 g/cm^3
ρ_{GaInSn}	6.3 g/cm^3
σ_{Cu}	6.0×10^7 $(\Omega\mathrm{m})^{-1}$
σ_{GaInSn}	3.5×10^6 $(\Omega\mathrm{m})^{-1}$
σ_{steel}	1.75×10^6 $(\Omega\mathrm{m})^{-1}$
B	4200 G

TABLE I. Experimental parameters of the physical system are displayed. The physical dimensions of the experimental apparatus, the differential rotation rates, the densities of the endcaps and working fluid, and the conductivities are summarized.

Experiment Split-Stable		Simulation Split-Stable		Simulation MRI	
Re	10^6	Re	1000	Re	1000
Rm	0.68	Rm	0.68	Rm	10
B_0	1.89	B_0	1.8	B_0	0.2
Λ	2.44	Λ	2.21	Λ	0.4

TABLE II. Dimensionless parameters of the system are displayed. The dimensionless parameters are the fluid Reynolds number, magnetic Reynolds number, axial magnetic field strength, and Elsasser number which corresponds to the viscosity of the system, the rotation rate, the background magnetic field, and the relative strength of the Lorentz force and Coriolis force respectively.

A. Split-Stable Case

Previous experimental results show that for insulating endcaps, an instability with azimuthal mode number $m = 1$ develops, caused by the formation of magnetized Stewartson-Shercliff layers (SSLs) driven by the background axial field above the threshold $\Lambda_{\mathrm{Ga}} > 1$ [28, 33]. The results from the non-axisymmetric simulations show the same general trend; after the background axial field is applied the azimuthal velocity becomes globally destabilized by the formation of free SSLs near the inner and outer ring boundary. These fluctuations culminate in Kelvin-Helmholtz like modes with an axially uniform structure and azimuthal mode structure transitioning from $m = 4$ to $m = 1$.

In Figure 4, we see the volumetrically averaged kinetic energy of the insulating endcap system without the background mean flow contribution. There is a modal cascade of power from $m = 4$ to $m = 1$ in the kinetic energy

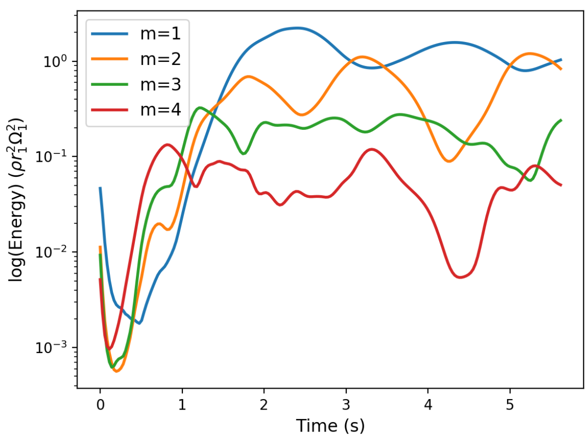

FIG. 4. Calculated volumetrically averaged kinetic energy contributions for the S-S insulating boundary simulations from azimuthal modes $m = 1$ to $m = 4$. Higher azimuthal modes are not active.

spectrum of the system, with the $m = 1$ contribution exponentially growing at early times. This qualitatively agrees well with the previous results with the emergence of a single dominant mode from initial multiple mode spectra [28, 33]. The non-axisymmetric contribution to the volumetric kinetic energy is resolved fully; kinetic energies from higher mode numbers $m > 4$ are orders of magnitude less than the $m \leq 4$ and do not contribute significantly to the volumetrically averaged kinetic energy.

Fluctuating azimuthal velocities $V_{\theta,\mathrm{fl}}$ were calculated by subtracting the time averaged mean flow V_{mean} from V_θ and plotted onto the azimuthal and axial plane. The mode structures depicted in Figure 5 clearly show the dominant $m = 1$ instability in the azimuthal cross-section at the midplane, indicating that the magnetized SSL produced a global instability throughout the bulk fluid rather than localized behavior near the endcaps. The instability also has an axially uniform profile.

In contrast to the gradual and coherent fluid response under insulating endcaps, the fluid response is much more dynamic and rapid when conducting boundaries are enforced. A comparison between the azimuthal velocities of the insulating and conducting endcaps after the background magnetic field is applied shows that there is an immediate response in the conducting case that leads to changes in the mean fluid flow and changes to the structural complexity of the azimuthal velocity fluctuations, while in the insulating case the fluctuations develop more gradually and are more structured. The $m = 1$ mode eventually dominates in the insulating case, but plots of the modal structure of the conducting case show that after the initial change in mean flow the fluctuations maintain an apparent azimuthal structure of $m = 2$.

The volumetrically averaged kinetic energy graph is shown in Figure 6 for the conducting boundaries. Comparing to the insulating case, the onset of instabilities in the conducting boundaries case is much more rapid and diverse. Although the strength of the modal fluctuations is weaker at a normalized value of $0.1 \sim 0.2$, there is no single mode that contributes dominantly to the kinetic energy; rather, multiple high-frequency modes contribute. However, the primary difference lies in the $m = 0$ axisymmetric evolution. In the conducting case, we see an immediate increase in the $m = 0$ kinetic energy which translates to a sudden change in the mean flow of the system compared to the insulating case where the mean flow doesn't change drastically. The inset in Figure 6b shows the change in the bulk flow as the $m = 0$ growth sets in; the strong shear is rapidly established as the total energy in the bulk flow is established.

Because the azimuthal velocity V_θ includes the $m = 0$ background mean flow, the radial (V_r) and axial (V_z) velocity perturbations were visualized instead to look at the mode structure of the instabilities. Figure 7 shows the azimuthal and axial mode structures of the instability. There is a clear $m = 0$ structure in both the radial and axial components of velocity. There seems to also be some modal breakdown into higher frequency in localized parts of the system near the axial boundaries, indicating that the system is evolving quickly and transitioning from the linear phase to the turbulent phase. The axial cross-sections show coherent structures in the meridional plane; most noticeably we have four circulatory cells that span the axial plane when the instability is saturated. The drastically different mode structure for the conducting boundaries suggests a completely different instability response mechanism compared to the insulating boundaries. For the insulating boundaries the instability culminated in K-H like modes with $m = 1$ and axially uniform mode structure, while for the conducting boundaries the resulting instability was an axisymmetric $m = 0$ mode with circulating cells in the meridional plane hinting at Rayleigh-like modes.

To investigate the difference between the conducting and insulating response, the current response to the background axial magnetic field is plotted in Figure 8. Almost immediately after the background magnetic field is turned on, large currents develop in the endcap boundaries for the conducting case. These thick boundary layer currents and the high conductivity of the endcaps lead to strong magnetic coupling of the fluid to the boundaries and result in significant return currents in the fluid volume itself. The large return currents ultimately drive strong azimuthal Lorentz forces and Maxwell stresses that reinforce the fluid rotation in the inner fluid volume while decreasing the rotation of the outer fluid volume, resulting in a sharp shear that drives the system to a Rayleigh unstable state. In contrast, this effect is not observed in the insulating case where the endcaps are treated as part of the vacuum; a small volume of fluid along the boundary interface forms a thin layer on the fluid/vacuum interface, effectively taking the place of the conducting endcaps. However, the low conductivity and small current layer thickness results in a much weaker

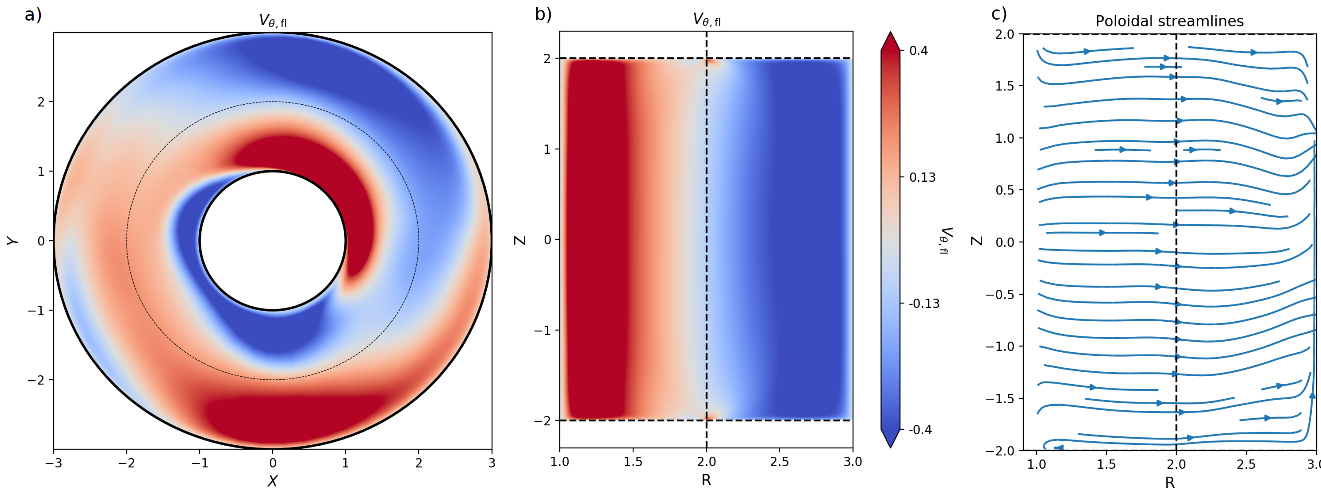

FIG. 5. The mode structures of the Split-Stable insulating simulation calculated for the normalized fluctuating azimuthal velocity $V_{\theta,\mathrm{fl}} = (V_\theta - V_{\mathrm{mean}})/V_{\mathrm{mean}}$. a) shows the azimuthal mode structure at the midplane ($z = 0$) and b) the axial (r-z) mode structure and streamlines at the azimuthal cross section $\theta = \pi/2$. The computational data was taken at $t = 2.1$ s when the $m = 1$ contribution was dominant.

coupling between the boundary and fluid compared to fully conducting boundaries. This culminates as minimal return currents that do not significantly increase the flow shear of the system, and remains stable to Rayleigh instabilities while still unstable to the magnetic Kelvin-Helmholtz instability for the insulating boundaries as reported previously [27, 28].

The effect of the Lorentz forces on the hydrodynamic stability of the system in both the conducting and insulating case can be seen in Figure 9, where the shear profile $q = -\partial \ln \Omega / \partial \ln r$ for various timescales are plotted. Almost immediately after application of the background field ($t = 0.1$ s), a localized peak that is above the Rayleigh stability threshold of $q = 2$ appears in the shear profile for the conducting boundaries, while the shear profile for the insulating boundaries remain relatively unchanged. This leads to an immediate growth in the Rayleigh-like structures shown in Figure 7 for the conducting case. For the insulating case, the development of shear is very slow; the shear eventually does go above the Rayleigh unstable limit at later times ($t = 0.7$ s) but the onset of K-H modes forces the shear profile back below the $q = 2$ threshold.

The late time shear profiles for the simulations and experiments are plotted in Figure 10. The shear in the insulating endcap simulations stays below $q = 2$ after the development of the K-H like mode except at the inner and outer cylinder boundaries where viscous forces play a large role. The shear in the conducting simulations shows localization of the shear above the Rayleigh stability threshold $q = 2$ between the radii $r = 1.6$ and $r = 2.5$. Referring back to Figure 7, we observe that the conducting $m = 0$ mode structure is also localized around these radii where $q > 2$, indicated in light dashed lines, supporting the onset of hydrodynamically unstable Rayleigh modes. Experimentally, similar q profiles are seen in the conducting case; the same large shear is established between $r = 1.6$ and $r = 2.5$. In the insulating case the shear also stays well below $q < 2$, but the shear profile deviates from the numerical values. This is probably because viscous forces are nontrivial in the insulating case and the computational restraints on fluid Reynolds number, which is 1/1000 that of the experiment, impact the flow dynamics.

The difference in response for the conducting and insulating boundaries can be understood through the work done on line-tied K-H instabilities by Miura *et al.* [36]. Although the stability analysis done by Miura *et al.* is for an infinite slab geometry with vertical boundaries of finite thickness and conductivity, a rough estimate for the stability of the cylindrical system can be extrapolated by transforming the longitudinal coordinate to the azimuthal coordinate. Modifying Eq. 36 in this paper for our cylindrical system gives the linear growth rate γ of line-tied K-H modes for finite axial wavenumbers:

$$\gamma^2 = m^2(V_\theta/r_1)^2 - k_z^2 V_A^2 \tag{1}$$

Using the values $m = 1$, $V_\theta/r_1 = 33.5\mathrm{rad/s}$, $k_z = \pi/28\mathrm{cm}$, $V_A = 4.5\mathrm{m/s}$, the growth rate γ^2 is negative, indicating that the K-H mode is stabilized in the conducting boundary system. Note that we have used the shortest axial wavelength due to the line-tied boundary condition. The mode structures with nonzero k_z that are demanded by the line-tied conducting axial boundaries contribute to magnetic field bending and stabilize the K-H modes.

However, in the insulating case, the most unstable K-H mode is associated to $k_z \sim 0$ resulting in the linear

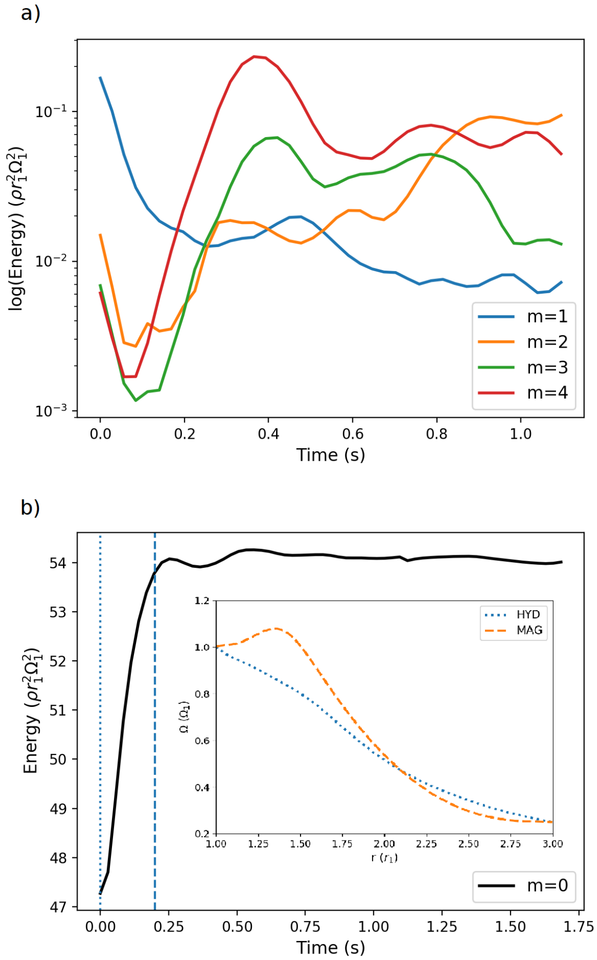

FIG. 6. Calculated volumetrically averaged kinetic energy contributions for conducting boundary S-S simulations. a) Azimuthal modes $m = 1$ to $m = 4$ b) $m = 0$, inset shows the flow profile before initialization and after the $m = 0$ mode growth. Higher azimuthal modes are not active.

growth rate in Eq. 40 of Ref. [36]:

$$\gamma = -\mu_0(\sigma_{\mathrm{GaInSn}} d)V_A^2/h + [(\mu_0(\sigma_{\mathrm{GaInSn}} d)V_A^2/h)^2 + m^2(V_\theta/r_1)^2]^{1/2} \quad (2)$$

Using the values of m, V_θ/r_1, V_A listed above, the conductivity of the fluid layer $\sigma_{\mathrm{GaInSn}} = 3.5 \times 10^6 (\Omega\mathrm{m})^{-1}$, and the value $d = 0.14$cm as a rough estimate of the layer width using the current profiles in Figure 8, the theoretical growth rate is $\gamma_{\mathrm{th}} = 33.1\ \mathrm{s}^{-1}$. Analyzing the growth rate of the line-tied K-H instability in the insulating simulations from Figure 4 gives the numerical growth rate $\gamma_{\mathrm{sim}} = 4.8\ \mathrm{s}^{-1}$. Despite the differences in the initial configuration (slab vs. cylindrical) and instability stage (local linear theory vs. global nonlinear simulations), the linear theory presented by Miura *et al.* qualitatively agrees with the results of the simulations, predicting suppression of line-tied K-H modes in the conducting case and the growth of said modes in the insulating case. Modification of the line-tied K-H theory for the cylindrical geometry in the MRI experiments remains for a future work.

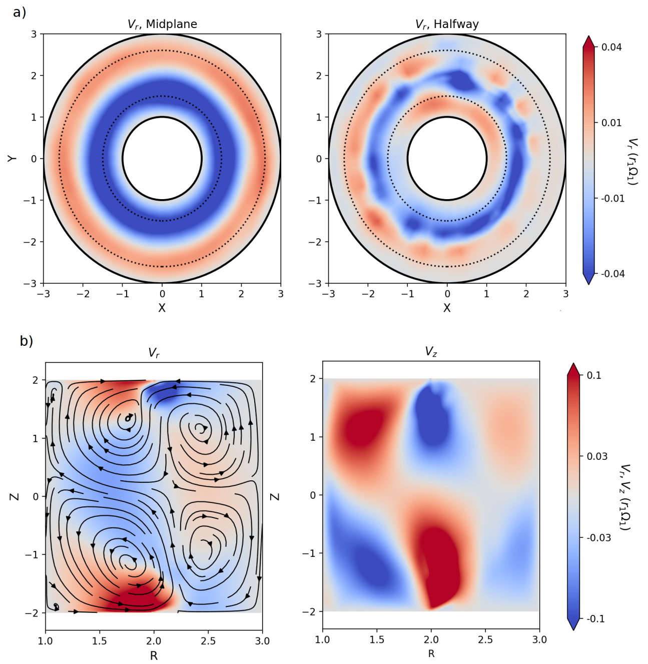

FIG. 7. The mode structures of the S-S conducting simulation calculated for the fluctuating radial and axial velocity V_r, V_z. a) shows the azimuthal mode structure of V_r at the midplane ($z = 0$) and halfway to the axial boundaries ($z = 1$), b) the axial mode structures of V_r, V_z, and streamlines at the azimuthal cross section $\theta = \pi/2$. The data was taken at $t = 0.1$ s when the $m = 0$ contribution is growing rapidly.

B. Reference MRI Unstable Case

3D non-axisymmetric simulations of the MRI unstable configuration with conducting boundaries are conducted to compare with the previous 2D results and the aforementioned split-stable state. Because we expect only the MRI to be unstable in this particular region, the eigenstructures and energy evolution of the MRI unstable configuration should be significantly different from the split-stable configuration, which is shown above to be hydrodynamically unstable.

The volumetrically averaged B_r, called the MRI signal, measures the change in the radial magnetic energy and is plotted for both the split-stable case and the MRI unstable case in Figure 11. The starting values of the MRI signal are different because the split-stable case is initialized with an experimentally relevant rotation profile with perturbations in V_r, which in turn imparts a nontrivial B_r when the background field is turned on. The MRI signal starts near zero for the MRI unstable case because a piecewise solid body initial state was used with no V_r. The saturated value of the MRI signal in the 3D non-

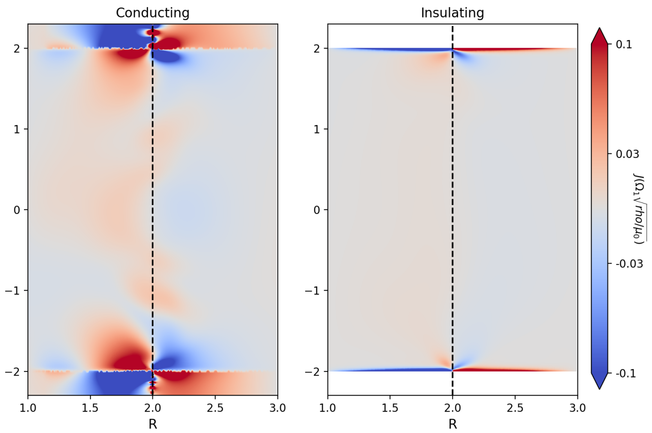

FIG. 8. The current responses J_r to the background magnetic field for the S-S conducting and insulating simulations. The current response and resulting Lorentz forces are strong and immediate for conducting case while the current response is weak for the insulating case.

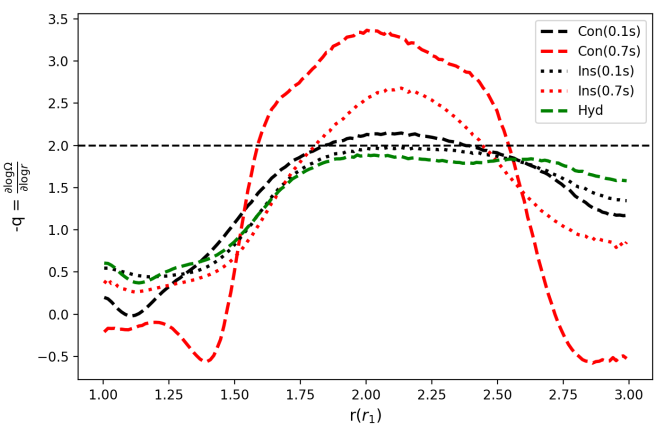

FIG. 9. $q = -\partial \ln \Omega / \partial \ln r$ plots at times $t = 0.1$ s colored in black and $t = 0.7$ s colored in red, taken at the midplane for the S-S simulations. The hydrodynamically stable initial state is colored in green. Early time behavior suggests that the response of the shear is rapid in the conducting case, while it is slower for the insulating case. Later time behavior has the shear above the Rayleigh threshold $q = 2$ for both the conducting and insulating cases, but the increased shear is maintained in the conducting case while it is flattened for the insulating case as the K-H mode develops.

axisymmetric simulations is identical to the 2D simulations, implying that only the axisymmetric $m = 0$ component is present. Furthermore, we can see that for the MRI unstable case the MRI signal grows with a saturated state orders of magnitude greater than the counterpart in the split-stable case. This is not surprising because the dominant instability in the split-stable case is hydrodynamically driven, while MRI is magnetically driven. Interestingly enough, the MRI signal in the split-stable case exponentially decays and gives rise to hydrodynamic instabilities.

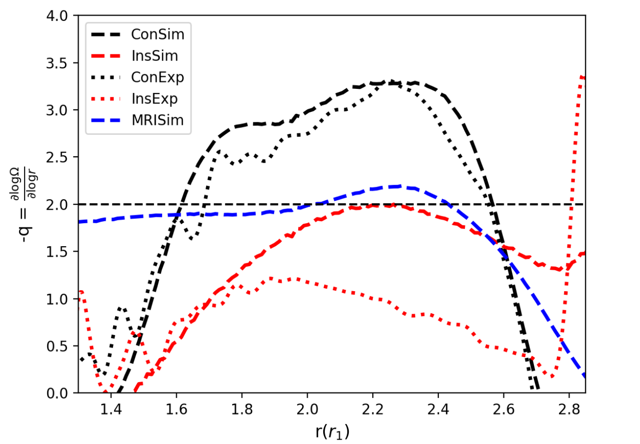

FIG. 10. $q = -\partial \ln \Omega / \partial \ln r$ plots versus radius at late times, taken at the midplane for the S-S simulations and experiments. q values above 2 are linearly unstable to Rayleigh's centrifugal instability. The black line indicates the q profile of the conducting endcaps, while the red line indicates the q profile of the insulating endcaps. The blue line indicates the q profile of the MRI unstable configuration with conducting endcaps.

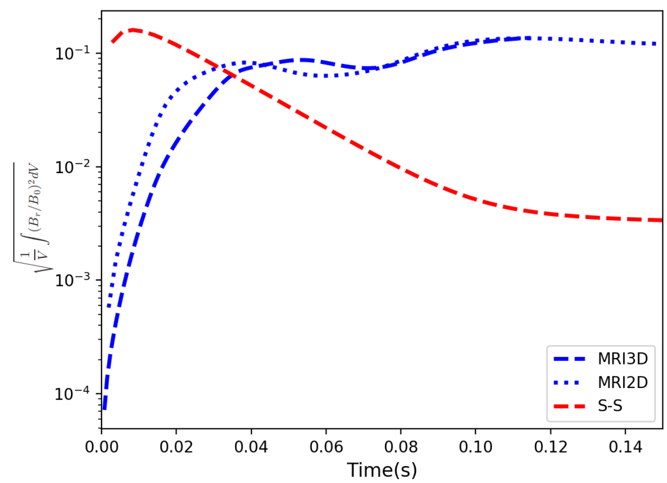

FIG. 11. The evolution of volumetrically averaged B_r (MRI signal) for the MRI unstable and S-S simulations. The MRI signal saturates at a much higher threshold in the MRI unstable configuration compared to the split-stable configuration. Slight differences in the MRI signal evolution for the 2D and 3D case is due to computational mesh size; the 3D simulations are conducted with a mesh that is 4 times finer so the initial perturbation is smaller than the 2D simulations.

The axial and azimuthal breakdown of the mode structures of the MRI unstable case also highlights the difference between these two configurations. Figure 12 shows the meridional cross-section of B and V for the MRI unstable case. Comparisons with previous 2D results [29] yield identical axial mode structures for the 2D and 3D case. Comparing the axial structures of the MRI unstable case with the split-stable case (*cf.* Figure 7) shows that there is a clear difference in the axial mode structure, indicating that the instability mechanism is different. In particular, the streamlines of V of the split-stable case resembles four vortices while in the MRI unstable case there are only two vortices on top of each other and spanning the entire radius of the system.

Figure 13 shows the relevant azimuthal mode structures of V_r and B_r of the split-stable configuration and the MRI unstable configuration. The velocity fluctuations are vastly different as expected by the change in parameter space; it is interesting to note that the shear profile of the MRI unstable configuration goes slightly over the centrifugal instability threshold $q = 2$ (*cf.* Figure 8). However, the spatial location of the $m = 0$ amplitude in the mode structure of V_r do not overlap with the region of increased shear, suggesting that the centrifugal modes are subdominant. In contrast, B_r has a large active $m = 0$ component orders of magnitude greater than the mostly dormant split-stable counterpart, as expected for the axisymmetric MRI perturbations.

IV. CONCLUSION

The effects of boundary endcap conductivity on a free Stewartson-Shercliff in the Princeton MRI Experiment were explored using 3D non-axisymmetric computational simulations. We find that the instabilities resulting from the formation of the free SSLs are global Kelvin-Helmholtz like modes with insulating axial boundaries, while the instabilities resulting from conducting axial boundaries are Rayleigh-like modes. The difference is attributed to the strong coupling of the conducting axial boundary with the working fluid; the immediate evolution of thick boundary layer currents in the endcaps lead to return currents in the fluid and stronger coupling, resulting in a strong azimuthal force that ultimately reinforces the flow shear. The increased shear causes the formation of quick Rayleigh modes with finite k_z in the conducting case. In the insulating case, the shear development is too slow to support Rayleigh-like mode growth, thus the most unstable K-H modes with zero axial wave number ($k_z = 0$) grow.

In summary, we find that the simulation results with insulating and conducting axial boundaries are consistent with previous experimental measurements [33] using a split-stable rotation profile to enforce large shear in the fluid domain. Our preliminary 3D simulation of the MRI unstable state also shows that there are significant differences in the velocity fluctuations compared to the split-stable case suggesting different instability mechanisms as expected. The magnetic field fluctuations show a strong dominant $m = 0$ component and an increasing MRI signal, which is a promising precursor for MRI.

As experiments and simulations in the MRI unstable regime are carried out, it is important to differentiate between the Rayleigh-like instability and the MRI. Current experimental efforts aim towards minimizing the formation of these SSLs by adjusting the individual rotation rates of the inner and outer rings so that the background hydrodynamic flow becomes flatter to avoid Rayleigh instabilities. Moving forward, it will be important to consider 3D non-axisymmetric simulations near the stability threshold for experimental relevance and direct comparisons.

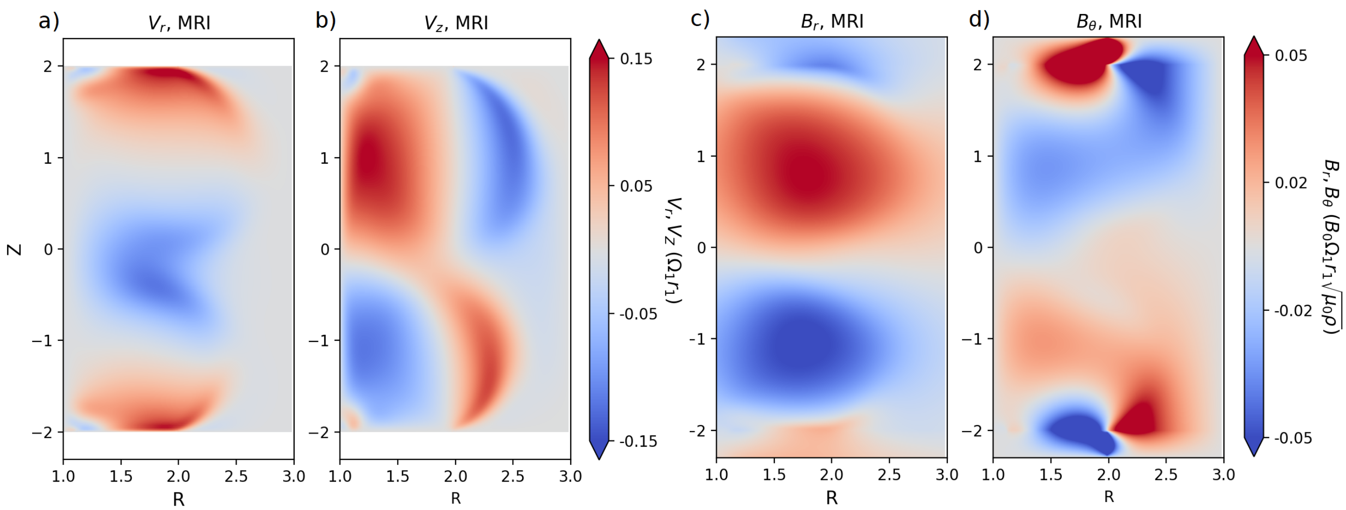

FIG. 12. Axial (r-z) mode structures of a) V_r, b) V_z, c) B_r, d) B_θ for the reference MRI unstable simulation. Structures remain axisymmetric even in the presence of non-axisymmetric modes in the simulations.

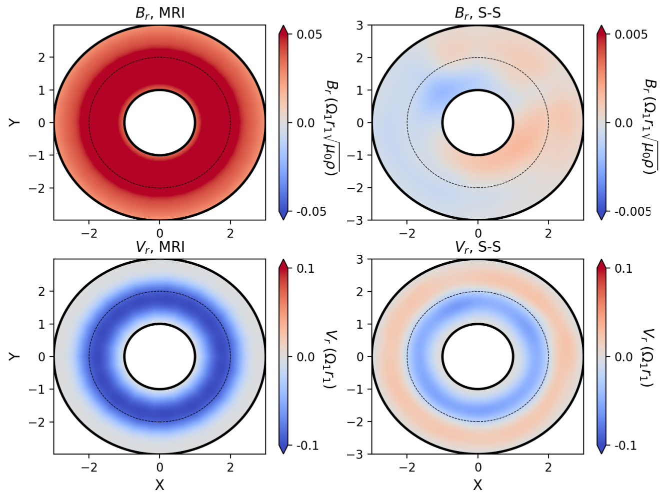

FIG. 13. Azimuthal mode structures of B_r and V_r of the S-S and MRI unstable simulations. Mode structures of V_r are similar in both cases with differences in radial distributions. The azimuthal mode structures of B_r and V_r of the MRI unstable configuration and the split-stable configuration are vastly different from each other, with a strong, dominant axisymmetric m=0 component in the MRI unstable configuration compared to a weak fluctuation in the split-stable configuration.

[1] Shakura, N. I., & Sunyaev, R. A. 1973, Astron. Astrophys, 24, 337
[2] Pringle, J. E. 1981, Ann. Rev. Astron. Astrophys., 19, 137
[3] J. F. Hawley, S. A. Balbus, 1998, Rev. Mod. Phys., 70, 1.
[4] J. F. Hawley, S. A. Balbus, and W. F. Winters, Astrophys. J. 518, 394 (1999)
[5] H. Ji, M. Burin, E. Schartman, and J. Goodman, Nature (London) 444, 343 (2006)
[6] E. M. Edlund and H. Ji, Phys. Rev. E 89, 021004(R) (2014).
[7] R. V. E. Lovelace, H. Li, S. A. Colgate, and A. F. Nelson, Astrophys. J. 513 (1999)
[8] G. Lesur, J.C.B. Papaloizou, Astron.Astrophys. 513 (2010)
[9] R. P. Nelson, O. Gressel and O. M. Umurhan, MNRAS 435 (2013)
[10] Velikhov, E. P. 1959, Sov. Physics JETP, 36, 995.
[11] S. A. Balbus and J. F. Hawley, Astrophys. J. 376, 214 (1991)
[12] S. Balbus and J. Hawley, Rev. Mod. Phys. 70, 1 (1998)
[13] H. Ji, J. Goodman, and A. Kageyama, R. Astron. Soc. 325, L1 (2001)
[14] M. D. Nornberg, H. Ji, E. Schartman, A. Roach, and J. Goodman, Phys. Rev. Lett. 104, 074501 (2010).
[15] Goodman J., Ji H., 2002, J. Fluid Mech., 462, 365
[16] Rüdiger G., Schultz M., Shalybkov D., 2003, Phys. Rev. E, 67, 046312
[17] Kageyama A., Ji H., Goodman J., Chen F., Shoshan E., 2004, J. Phys. Soc. Japan, 73, 2424
[18] Noguchi K., Pariev I., Colgate S., Nordhaus J., 2002, Astrophys. J., 575, 1151
[19] Sisan D., Mujica N., Tillotson W., Huang Y.-M., Dorland W., Hassam A., Antonsen T., Lathrop D., 2004, Phys. Rev. Lett., 93, 114502
[20] Stefani F., Gundrum T., Gerbeth G., Rüdiger G., nd J. Szklarski M. S., Hollerbach R., 2007, Phys. Rev. Lett., 97, 184502
[21] F. Ebrahimi, B. Lefebvre, C. B. Forest, A. Bhattacharjee, Physics of Plasmas 18, 062904 (2011)
[22] J. L. Guermond, R. Laguerre, J. Leorat, and C. Nore, J. Comput. Phys. 228, 2739 (2009)
[23] V. W. Ekman, Arch. Math. Astron. Phys. 2, 1 (1905)
[24] K. Stewartson, J. Fluid Mech. 3, 1 (1957)
[25] J. Hartmann, Mat. Fys. Medd. 15, 1 (1937)
[26] J. A. Shercliff, Math. Proc. Cam. Phi. Soc. 49, 136 (1953)
[27] C. Gissinger, J. Goodman, and H. Ji, Phys. Fluids 24, 074109 (2012)
[28] A. H. Roach, E. J. Spence, C. Gissinger, E. M. Edlund, P. Sloboda, J. Goodman, and H. Ji, Phys. Rev. Lett. 108, 154502 (2012)
[29] X. Wei, H. Ji, J. Goodman, F. Ebrahimi, E. Gilson, F. Jenko, and K. Lackner, Phys. Rev. E 94, 063107 (2016)
[30] J. Szklarski, Astron. Nachr. 328, 499-506 (2007)
[31] J. Szklarski, G. Gerbeth, Astron. Nachr. 329, 667-674 (2008)
[32] F. Stefani, G. Gerbeth, T. Gundrum, R. Hollerbach, J. Priede, G. Rüdiger, J. Szklarski, Phys. Rev. E 80, 066303 (2009)
[33] K. Caspary, D. Choi, F. Ebrahimi, E. Gilson, J. Goodman, H. Ji, Phys. Rev. E 97, 063110 (2018)
[34] E. J. Spence, A. H. Roach, E. M. Edlund, P. Sloboda, and H. Ji, Phys. Plasmas 19, 056502 (2012)
[35] E. Schartman, H. Ji and M. Burin, Rev. Sci. Instrum. 80, 024501 (2009)
[36] A. Miura, J. R. Kan, Geophys. Res. Lett. 19, 15 (1992)